

Article

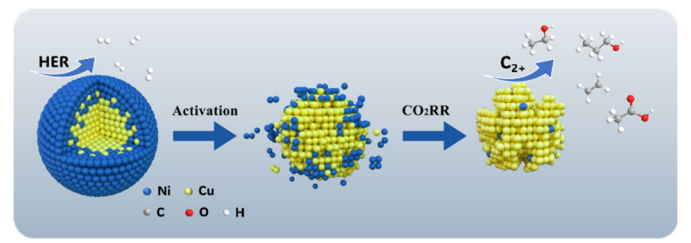
# Cathodic Corrosion-Induced Structural Evolution of CuNi Electrocatalysts for Enhanced CO<sub>2</sub> Reduction

Wenjin Sun <sup>1,†</sup>, Bokki Min <sup>2,†</sup>, Maoyu Wang <sup>3</sup>, Xue Han <sup>4</sup>, Qiang Gao <sup>1</sup>, Sooyeon Hwang <sup>5</sup>, Hua Zhou <sup>3</sup>, and Huiyuan Zhu <sup>1,2,\*</sup>

- <sup>1</sup> Department of Chemistry, University of Virginia, Charlottesville, VA 22904, USA
- Department of Chemical Engineering, University of Virginia, Charlottesville, VA 22904, USA
- <sup>3</sup> Advanced Photon Source, Argonne National Laboratory, Lemont, IL 60439, USA
- Department of Chemical Engineering, Virginia Polytechnic Institute and State University, Blacksburg, VA 24061, USA
- <sup>5</sup> Center for Functional Nanomaterials, Brookhaven National Laboratory, Upton, NY 11973, USA
- Correspondence: kkx8js@virginia.com
- <sup>†</sup> These authors contributed equally to this work.

Received: 22 October 2024; Revised: 25 November 2024; Accepted: 27 November 2024; Published: 4 December 2024

**Abstract:** The electrochemical CO<sub>2</sub> reduction reaction (CO<sub>2</sub>RR) has attracted significant attention as a promising strategy for storing intermittent energy in chemical bonds while sustainably producing value-added chemicals and fuels. Copper-based bimetallic catalysts are particularly appealing for CO<sub>2</sub>RR due to their



unique ability to generate multi-carbon products. While substantial effort has been devoted to developing new catalysts, the evolution of bimetallic systems under operational conditions remains underexplored. In this work, we synthesized a series of  $Cu_xNi_{1-x}$  nanoparticles and investigated their structural evolution during  $CO_2RR$ . Due to the higher oxophilicity of Ni compared to Cu, the particles tend to become Ni-enriched at the surface upon air exposure, promoting the competing hydrogen evolution reaction (HER). At negative activation potentials, cathodic corrosion has been observed in  $Cu_xNi_{1-x}$  nanoparticles, leading to the significant Ni loss and the formation of irregularly shaped Cu nanoparticles with increased defects. This structural evolution, driven by cathodic corrosion, shifts the electrolysis from HER toward  $CO_2$  reduction, significantly enhancing the Faradaic efficiency of multicarbon products  $(C_{2+})$ .

Keywords: electrochemical CO<sub>2</sub> reduction; bimetallic; nanoparticles; cathodic corrosion; structural evolution

#### 1. Introduction

With the rapid rise in CO<sub>2</sub> emissions and growing global energy demand, the electrochemical CO<sub>2</sub> reduction reaction (CO<sub>2</sub>RR) has attracted widespread interest as a promising strategy to close the carbon cycle by converting CO<sub>2</sub> into valuable chemicals and fuels [1–3]. Extensive research has been devoted to CO<sub>2</sub>RR catalysts in recent years, particularly Cu-based catalysts, which exhibit a unique ability to convert CO<sub>2</sub> into multi-carbon products, such as C<sub>2</sub>H<sub>4</sub>, C<sub>2</sub>H<sub>5</sub>OH, and C<sub>3</sub>H<sub>7</sub>OH. These multi-carbon products offer higher energy density and greater market value compared to single-carbon products [4–8]. This unique property is closely associated with the moderate \*CO adsorption energy on Cu, which balances the activation of CO<sub>2</sub> and the subsequent hydrogenation of \*CO intermediate [5,9]. However, Cu still faces challenges such as poor selectivity, high overpotential, and competition from the hydrogen evolution reaction (HER) [10,11]. To overcome these limitations, various strategies—such as alloying [12–14], tuning the oxidation state [15,16], and surface/interface modification [17,18]—have been explored to modulate the physicochemical properties of Cu.

Constructing bimetallic catalysts has emerged as an effective strategy for improving CO<sub>2</sub>RR performance by harnessing the synergistic effects between Cu and a secondary metal [13,19,20]. For instance, AgCu bimetallic catalysts employ a tandem catalysis strategy, where the reaction is partitioned into distinct steps, each facilitated by different catalytic sites [21,22]. Additionally, the compressive strain exerted on Cu by the CuAg surface alloy exemplifies the bimetallic synergistic effect in CO<sub>2</sub>RR. This strain reduces the surface coverage of adsorbed



hydrogen (\*H) and decreases oxophilicity, thereby improving catalytic performance [23]. Alloying can also refine catalytic performance. The Cu-Ni alloy, for instance, exhibits synergistic Cu-Ni active sites that increase \*H coverage, facilitating the hydrogenation of adsorbed \*CO into C<sub>1</sub> products. This leads to a gradual shift from the production of CO and C<sub>2</sub> species toward an increased formation of CH<sub>4</sub> and HCOO<sup>-</sup> [14].

While numerous Cu-based bimetallic catalysts have been studied, maintaining their structural stability under CO<sub>2</sub>RR conditions remains a significant challenge [24,25]. The application of potential bias, along with exposure to electrolytes, CO2, and reaction intermediates, can induce substantial changes in catalyst structures. These changes, often involving atomic rearrangement or alterations in chemical states [26], ultimately lead to the reconstruction of active sites [9,27,28], which can significantly impact catalytic performance. Unfortunately, the dynamic evolution of bimetallic systems is often overlooked, resulting in a limited fundamental understanding of the true nature of the active sites. For example, polycrystalline Cu electrodes undergo facet evolution through stepwise surface reconstruction, initially forming Cu (111) within the first 30 min, followed by a transition to Cu (100) after an additional 30 min [29]. Cu is also prone to spontaneous oxidation in air and reduction under cathodic potential. The presence of Cu<sup>+</sup> and subsurface oxygen atoms is believed to contribute to the enhanced catalytic performance of oxide-derived (OD)-Cu [30]. Subsurface oxygen can improve \*CO adsorption and promote subsequent C-C coupling; however, the precise nature and dynamic evolution of the true active sites remains elusive [16]. Using in-situ and operando techniques, Vavra et al. observed that during the startup phase, dissolution and redeposition occur on the surface of Cu, resulting in an increase in particle size and changes in morphology, with Cu oxides playing a crucial role in this process [31]. Beyond redox reactions, Cu's high mobility under working conditions can result in leaching from electrodes. Chen et al. synthesized intermixed and phase-segregated AgCu nanoparticles (NPs) and found that both types evolved into structures with two distinct phases due to Cu's high mobility and poor Ag-Cu compatibility [32]. Another example is the Cu-Zn system, where cationic Zn species are reduced during the reaction, forming a CuZn alloy, which shifts selectivity from CH<sub>4</sub> (over Cu-ZnO) to CO (over the CuZn alloy) [33]. Overall, the dynamic evolution of Cu-based bimetallic catalysts is anticipated to be more complex than that of pure metals, involving morphological changes, structural reconstruction, and variations in chemical state. This complexity arises from the competitive and coexisting processes of redox reactions, dissolution, and redeposition of multiple metal species.

In this work, we investigated the structural evolution of bimetallic  $Cu_xNi_{1-x}$  NPs with tunable composition under  $CO_2RR$  operating conditions. Our results reveal that these bimetallic catalysts undergo cathodic corrosion in  $CO_2RR$ , shifting selectivity from  $H_2$  evolution to  $CO_2$  reduction. Prior to cathodic activation, these catalysts exhibited a Ni-enriched surface due to Ni's high oxophilicity, resulting in over 90% Faradaic efficiency (FE) for  $H_2$ . Upon cathodic activation, the catalysts underwent surface reconstruction and changes in oxidation state, with Ni leaching out due to cathodic corrosion at working potentials, while Cu was simultaneously reduced. This process results in a roughened surface that exposed more metallic Cu active sites (Figure 1a), significantly enhancing the selectivity for multi-carbon products. By tuning the Cu and Ni composition and optimizing the cathodic activation steps, we found that  $Cu_xNi_{1-x}$  with a precursor ratio of  $Cu_{0.71}Ni_{0.29}$  achieved the highest  $C_{2+}$  FE of 42.5% at -1.4  $V_{RHE}$  (reversible hydrogen electrode, RHE), compared to 24.1% for pristine Cu at the same potential.

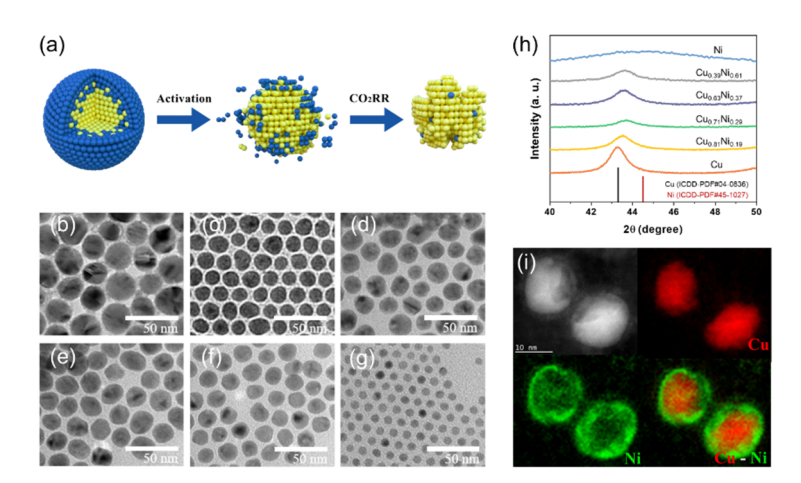


Figure 1. (a) Scheme of evolution behavior of  $Cu_xNi_{1-x}$  NPs upon cathodic corrosion and  $CO_2RR$ . TEM images of  $Cu_xNi_{1-x}$  NPs: (b) pure Cu, (c)  $Cu_{0.81}Ni_{0.19}$ , (d)  $Cu_{0.71}Ni_{0.29}$ , (e)  $Cu_{0.63}Ni_{0.37}$ , (f)  $Cu_{0.39}Ni_{0.61}$ , (g) pure Ni. (h) XRD patterns of  $Cu_xNi_{1-x}$  NPs. (i) The HAADF-STEM image and corresponding STEM-EELS elemental maps of  $Cu_{0.71}Ni_{0.29}$ .

#### 2. Result and Discussion

#### 2.1. Synthesis and Characterization of $Cu_xNi_{1-x}$

A series of Cu<sub>x</sub>Ni<sub>1-x</sub> NPs with varying Cu and Ni compositions were synthesized using a modified method [34], by adjusting the Ni precursor content (details provided in the Supporting Information). For comparison, pure Cu and Ni NPs were also synthesized using the same method. The composition of the assynthesized Cu<sub>x</sub>Ni<sub>1-x</sub> NPs was confirmed by inductively coupled plasma optical emission spectroscopy (ICP-OES) on a on a SPECTRO GENESIS ICP spectrometer (SPECTRO Analytical Instruments GmbH, Kleve, North Rhine-Westphalia, Germany) and designated as Cu, Cu<sub>0.81</sub>Ni<sub>0.19</sub>, Cu<sub>0.71</sub>Ni<sub>0.29</sub>, Cu<sub>0.63</sub>Ni<sub>0.37</sub>, Cu<sub>0.39</sub>Ni<sub>0.61</sub>, and Ni, respectively. Transmission electron microscope (TEM, Thermo Fisher Scientific, Waltham, MA, US) images (Figure 1b-g) reveal that the Cu<sub>x</sub>Ni<sub>1-x</sub> exhibit a spherical shape and uniform morphology, with average sizes ranging from 15 nm to 25 nm. Pure Cu has the largest size (25.4  $\pm$  6.0 nm), while Ni displays the smallest diameter (7.4  $\pm$  1.3 nm). Particle size generally decreases with increasing Ni content (Figure S1 and Table S1). The X-ray Diffraction (XRD, Philips Analytical, Westborough, MA, US) patterns of all the samples are presented in Figure S2. As shown in the magnified region (Figure 1h), the Cu (111) peak in Cu<sub>x</sub>Ni<sub>1-x</sub> gradually shifts from 43.3° to 44.5° with the incorporation of Ni, indicating a reduction in Cu lattice spacing [35]. The peak also broadens with increasing Ni content, consistent with the TEM results. Notably, due to Ni's higher oxophilicity compared to Cu, the  $Cu_xNi_{1-x}$ NPs tend to develop a Ni-enriched surface when stored under ambient conditions, as evidenced by the high-angle annular dark-field (HAADF) scanning transmission electron microscopy combined with electron energy loss spectroscopy (STEM-EELS, Hitachi, Tokyo, Japan) images and element mappings of Cu<sub>0.71</sub>Ni<sub>0.29</sub> (Figure 1i).

## 2.2. Cathodic Activation of $Cu_xNi_{1-x}$

Electrochemical experiments were conducted on all samples to assess their CO<sub>2</sub>RR performance, with detailed procedures provided in the SI. Prior to CO<sub>2</sub>RR, cathodic pre-treatment was employed to activate the working electrodes loaded with the as-synthesized NPs. Half of the electrodes were activated for 2 h at their optimal activation potential, while the untreated electrodes served as the control group. The difference in the CO<sub>2</sub>RR between the activated and control groups was used to evaluate the impact of activation on catalytic performance. Cathodic activation was performed at various potentials in a conventional H-cell, with a Pt foil serving as the anode and Ag/AgCl as the reference electrode, while CO2 was continuously bubbled at a rate of 10 sccm. Cyclic voltammetry (CV) was initially performed in Ar-saturated and subsequently in CO<sub>2</sub>-saturated solutions, with scans between -1.4 V<sub>RHE</sub> and 0 V<sub>RHE</sub> for 20 cycles at a scan rate of 20 mV/s to clean the surface of the electrocatalysts. For instance, CV cycles were performed on pure Cu electrode, and then the electrode activated at -1.0 V<sub>RHE</sub> for 2 h under continuous CO<sub>2</sub> flow (10 sccm). After activation, CV was performed again in both Arsaturated and CO<sub>2</sub>-saturated solutions. The treated electrode was then used for CO<sub>2</sub>RR at potentials from -1.0 V<sub>RHE</sub> to -1.4 V<sub>RHE</sub>, in 0.1 V intervals, with each potential step maintained for 1 h. This process was repeated for different activation potentials of -1.1 V<sub>RHE</sub>, -1.2 V<sub>RHE</sub>, and -1.3 V<sub>RHE</sub> (Figure S3). Figure 2a,b illustrate the product distribution and corresponding FEs for pure Cu before and after activation at −1.1 V<sub>RHE</sub> for 2 h. Notably, there is no substantial change in product distribution before and after activation. At the applied potential of -1.0 V<sub>RHE</sub>, the primary products of CO<sub>2</sub>RR on pure Cu before activation are formate, H<sub>2</sub>, and CO, with FEs of 50.3%, 37.7%, and 4.8%, respectively (Figure 2a). At the same potential after activation, the FEs of these products are 51.4%, 41.8% and 5.2%, which are close to those observed prior activation. This indicates that cathodic activation had minimal effect on the catalytic performance of pure Cu. The C2+ FE summarized in Figure 2c further confirms the negligible effect of the activation treatment on pure Cu, with only a slight increase in C2+ FE from 20.0% to 24.1% at -1.4 V<sub>RHE</sub> after activation, while the FEs of other products remain largely unchanged.

In contrast,  $Cu_{0.71}Ni_{0.29}$  exhibits a high  $H_2$  FE of over 90% at -1.0  $V_{RHE}$  before activation, which can be attributed to surface enrichment with Ni, leading to a notably low FE for  $CO_2RR$  products (Figure 2d). Electrodes loaded with  $Cu_{0.71}Ni_{0.29}$  were then activated at -1.2  $V_{RHE}$ , -1.3  $V_{RHE}$ , -1.4  $V_{RHE}$ , respectively. Taking the -1.3  $V_{RHE}$  activation as an example, the HER after activation was significantly suppressed, with the FE decreasing to 67.4% at -1.0  $V_{RHE}$  (Figure 2e). Products distribution shifts remarkably after activation, as evidenced by a substantial increase in  $CO_2RR$  efficiency. For instance, the formate FE rose from 5.8% to 29.4% at -1.0  $V_{RHE}$ , and the CO FE increased from 7.9% to 21.1% at -1.2  $V_{RHE}$ . As shown in Figure 2f and Table S4, after activation at -1.3  $V_{RHE}$ , the  $C_{2+}$  FE at -1.4  $V_{RHE}$  increased to 42.5%, the highest among all trials, establishing -1.3  $V_{RHE}$  as the optimal activation potential for  $Cu_{0.71}Ni_{0.29}$ . Additionally, a new liquid product, 1-propanol (1-PrOH), was detected with a FE of 12.6% at -1.4  $V_{RHE}$ . These results indicate that cathodic activation of  $Cu_{0.71}Ni_{0.29}$  effectively suppressed the HER while promoting the formation of  $C_{2+}$  product. A similar trend is observed for other  $Cu_xNi_{1-x}$ 

catalysts (Figures S4–S7). Based on these findings, we hypothesize that cathodic activation induces surface evolution or reconstruction in  $Cu_xNi_{1-x}$ , enhancing  $CO_2RR$  selectivity. In addition, the suppressed HER after activation suggests a plausible mechanism in which surface Ni atoms leach from catalysts, creating more surface defects under cathodic potentials.

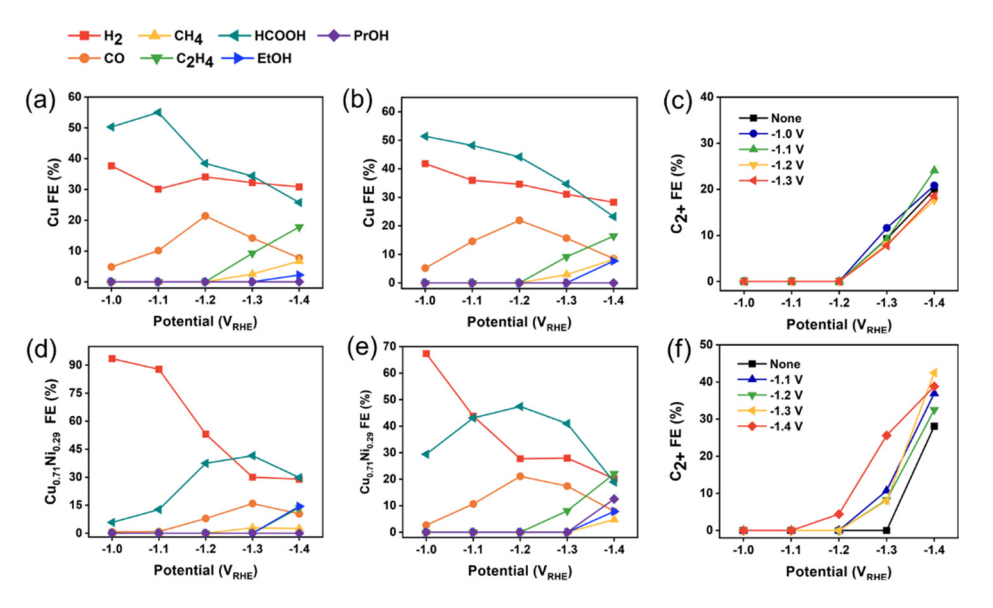


Figure 2. FEs of CO<sub>2</sub>RR on pure Cu before activation (a), and after activation (b) at -1.1 V<sub>RHE</sub> for 2 h. (c) C<sub>2+</sub> FEs on pure Cu after activation at different potentials. FEs of CO<sub>2</sub>RR on Cu<sub>0.71</sub>Ni<sub>0.29</sub> before activation (d), and after activation (e) at -1.3 V<sub>RHE</sub> for 2 h. (f) C<sub>2+</sub> FEs on Cu<sub>0.71</sub>Ni<sub>0.29</sub> after activation at different potentials.

## 2.3. CO2RR Performance

To comprehensively evaluate the composition effect, Figures 3, S8 and S9 summarize the activity and selectivity towards H<sub>2</sub>, C<sub>1</sub> and C<sub>2+</sub> of Cu<sub>x</sub>Ni<sub>1-x</sub> under different conditions. It is important to note that each catalyst was activated at its optimized activation potential. Notably, differences in product distribution were observed with changes in catalysts composition, applied potential, and the activation status. As shown in Figures 3a and S8, the Cu<sub>x</sub>Ni<sub>1-x</sub> catalysts generally exhibit higher geometric surface area-normalized total current density (j<sub>total</sub>) and partial current density for  $C_{2+}$  ( $j_{C2+}$ ) than pure Cu. The  $j_{C2+}$  increases with Cu content, highlighting the intrinsic activity of Cu for  $C_{2+}$  formation and the advantage of the bimetallic NPs over pure Cu.  $Cu_{0.81}Ni_{0.19}$  exhibits the highest  $j_{C_{2+}}$ as well as the highest FE before activation. After activation, Cu<sub>0.71</sub>Ni<sub>0.29</sub> achieved the highest C<sub>2+</sub> FE of 42.5%, compared to 24.1% of pure Cu at -1.4 V<sub>RHE</sub>, and the largest current density ratio of  $j_{C2+}/j_{H2}$  of 2.1 (Figure 3b). By reducing Ni content and increasing applied potential, CO<sub>2</sub>RR selectivity was enhanced, while HER was greatly suppressed both in pre-activated and after activated conditions (Figure S9). For instance, for pre-activated Cu<sub>0.63</sub>Ni<sub>0.37</sub>, as the potential shifts from -1.0 V<sub>RHE</sub> to -1.4 V<sub>RHE</sub>, the H<sub>2</sub> FE drops from 95.8% to 35.4%, while the C<sub>1</sub> FE increases from 2.0% to 32.6% and the C<sub>2+</sub> FE rises from 0 to 28.6%. Regarding the C<sub>2+</sub>, cathodic activation enhances the FE for all  $Cu_xNi_{1-x}$  compositions (Figure 3c). For example, for  $Cu_{0.71}Ni_{0.29}$ , after activation at -1.3 $V_{RHE}$ , the  $H_2$  FE decreases from 87.7% to 43.8% at -1.1  $V_{RHE}$  and from 28.9% to 20.2% at -1.4  $V_{RHE}$ , while the C<sub>2+</sub> FE increases from 28.1% to 42.5% at -1.4 V<sub>RHE</sub>. 1-PrOH was detected on Cu<sub>0.63</sub>Ni<sub>0.37</sub>, Cu<sub>0.71</sub>Ni<sub>0.29</sub>, and Cu<sub>0.81</sub>Ni<sub>0.19</sub> (Figure 3d). The optimization of detailed activation and reaction conditions in Figure 3d were listed in Tables S2–S6. These results suggest that the Cu<sub>x</sub>Ni<sub>1-x</sub> NPs with higher Cu content exhibit greater C<sub>2+</sub> activity and selectivity after activation, and the cathodic activation positively influence CO<sub>2</sub>RR. In the following discussion, we focus on the evolution behavior of Cu<sub>0.71</sub>Ni<sub>0.29</sub> NPs.

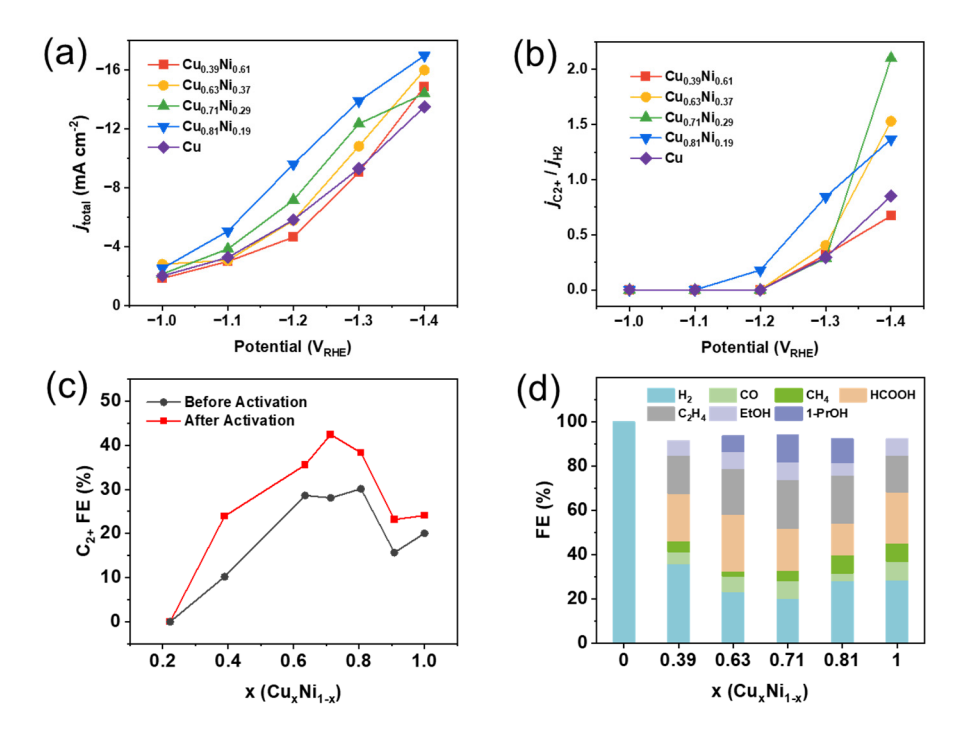


Figure 3. (a) The geometric surface area-normalized total current density ( $j_{total}$ ) at different applied potentials. (b) Partial current density ratio  $j_{C2+}/j_{H2}$ . (c)  $C_{2+}$  FE of  $Cu_xNi_{1-x}$ . (d) Products distribution after activation under the condition highlighted in Tables S2–S6.

## 2.4. In-Situ and Ex-Situ Characterization of the Structural Evolution of Cu<sub>x</sub>Ni<sub>1-x</sub>.

To elucidate the mechanisms driving the shift in selectivity, we employed *in-situ* and *ex-situ* techniques to investigate the structural evolution under working conditions. Figure 4 presents the STEM-EELS data, clearly showing a Ni-enriched surface (green) with a Cu core (red). According to the EELS data in Table S7, after 2 h of activation, both Ni and O content in Cu<sub>0.71</sub>Ni<sub>0.29</sub> decrease, with Ni dropping from 24.9% to 13.7%, while the Cu ratio increasing from 52.0% to 76.0%. This compositional change is further corroborated by ICP-OES results (Figure S10), which indicates that as the activation potential becomes more cathodic, the Ni loss of the electrode increases, while the Cu content rises. When the activation is performed at -1.4 V<sub>RHE</sub>, the Ni content loss reaches 90%. In addition, the change in morphology and composition persists during the subsequent reaction and become increasingly pronounced as the reaction progresses. After 5 h of CO<sub>2</sub>RR, nearly all Ni leaches off, resulting in an approximate absolute loss of 100% and the formation of a rougher surface with more defects. The morphology of NPs undergoes a significant transformation, adopting an irregular shape (Figures 4k-m), similar to the morphological changes observed in the pure Cu (Figure S11). Regarding the observed cathodic corrosion and dissolution, recent studies suggest that pure Cu can form dissolvable ternary hydrides under CO<sub>2</sub>RR conditions at extremely negative potentials, aided by alkali cations [36]. Another possible mechanism for Cu's structural evolution involves the formation of transient Cu-carbonyls and Cu-oxalates [27]. Our observations indicate that Cu<sub>x</sub>Ni<sub>1-x</sub> catalysts with a Ni-enriched surface predominantly produce H<sub>2</sub> via the HER in the absence of electrochemical activation. Given that Ni is more susceptible to corrosion in CuNi solid solutions, as indicated by the Pourbaix diagram [37], it is plausible that Ni undergoes an H2-induced and/or ternary hydride pathway [38], leading to its dissolution into the electrolytes. Notably, unlike Cu, which tends to redeposit onto the parent material [31,32], Ni remains in the electrolyte without re-deposition onto the electrode (Figure S10) [39].

In-situ X-ray absorption spectroscopy (XAS) was performed to monitor the evolution of the chemical state of Cu<sub>0.71</sub>Ni<sub>0.29</sub> and pure Cu at relevant potentials. Figures 5 and S12–S18 present the normalized Cu and Ni K-edge spectra from X-ray absorption near-edge spectroscopy (XANES) and Fourier-transformed extended X-ray absorption fine structure (EXAFS) spectra, along with fitting results. The XANES spectra show that the absorption edges of both Cu<sub>0.71</sub>Ni<sub>0.29</sub> and pure Cu shift to higher energy direction compared to Cu foil, with Cu<sub>0.71</sub>Ni<sub>0.29</sub> being closer to Cu foil (Figure 5a,b), indicating that Cu in Cu<sub>0.71</sub>Ni<sub>0.29</sub> is less oxidized than that in pure Cu. Under activation conditions, the edge positions shift to lower energy direction, approaching that of Cu foil, which suggests reduction upon activation. In the R space (Figures 5c,d and S12), two distinct peaks at 1.5 Å and 2.2 Å correspond to Cu-O and Cu-Cu/Ni coordination, respectively [40]. Due to the similar atomic radius of Cu and Ni (2.552 Å and 2.488 Å, respectively), it is challenging to distinguish between Cu-Ni and Cu-Cu coordination. While

no significant peak shifts are observed, the increased intensity of the Cu-Cu/Ni coordination and the diminished Cu-O signal confirms a transition from the oxidized to metallic state upon cathodic activation. Additionally, the difference in R space between pure Cu and Cu<sub>0.71</sub>Ni<sub>0.29</sub> further confirms the higher oxidation state of pure Cu (Figure S12). EXAFS fitting (Figure S14–S18, Table S8–S10) provides quantitative insights into the coordination environment of Cu and Ni. At open circuit potential (OCP), the coordination numbers (CNs) of Cu-Cu/Ni for Cu<sub>0.71</sub>Ni<sub>0.29</sub> and pure Cu are 9.28 and 5.54 (Figure 5e), respectively, indicating that a predominantly metallic Cu state in Cu<sub>0.71</sub>Ni<sub>0.29</sub>. After activation, the CNs increase to over 10 for both catalysts and remain stable throughout reaction process, with Cu<sub>0.71</sub>Ni<sub>0.29</sub> exhibiting slightly higher CNs than pure Cu. In the zoomed R space (Figure 5f), a slight peak shift in Cu-O and Cu-Cu/Ni is observed for Cu<sub>0.71</sub>Ni<sub>0.29</sub> compared to pure Cu and Cu foil. The peak positions for pure Cu are close to those of Cu foil, while those of Cu<sub>0.71</sub>Ni<sub>0.29</sub> shift to shorter radial distances, indicating the presence of residual Ni after activation and reaction under the most cathodic potential, as shown in ICP results (Figure S10). Compared to the pre-activated Cu<sub>0.71</sub>Ni<sub>0.29</sub> catalysts, this extremely low concentration of Ni residue, along with the structural defects and roughened Cu surface, may play a role in promoting CO<sub>2</sub> adsorption and reduction during the CO<sub>2</sub>RR. For Ni, the shift of the absorption edge to higher energy at OCP followed by a subsequent shift to lower energy after activation (Figure S13) suggests the presence of Ni oxides and their subsequent reduction. As the potential becomes more negative, Ni transitions into a more metallic state, as evidenced by the increase in Ni-Cu peak intensity in R space and Ni-Ni/Cu CN. Collectively, the Cu in Cu<sub>0.71</sub>Ni<sub>0.29</sub> is largely protected from oxidation by Ni-enriched surface. During activation, Ni leaches from the catalyst surface due to cathodic corrosion, allowing Cu to be reduced to its metallic state. This process creates structural defects and roughness on the Cu surface, potentially enhancing CO<sub>2</sub> adsorption and catalytic activity. The residual Ni likely stabilizes the metallic Cu state and provides additional active sites [41].

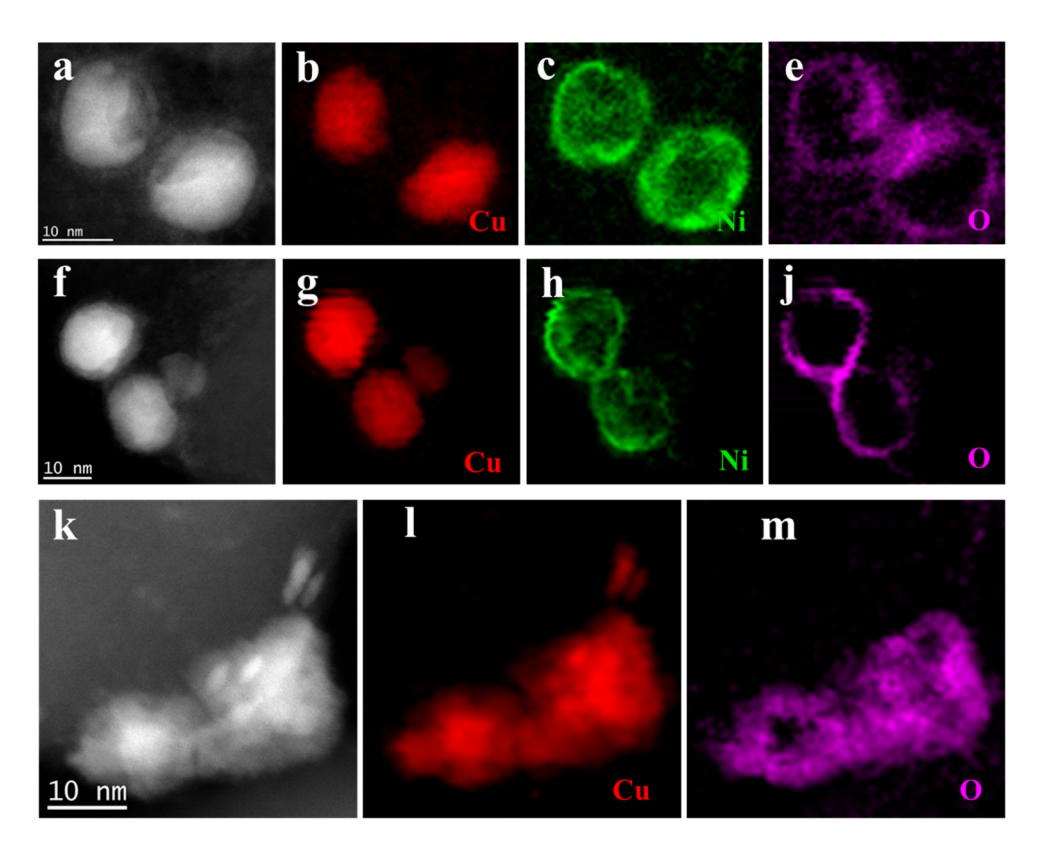
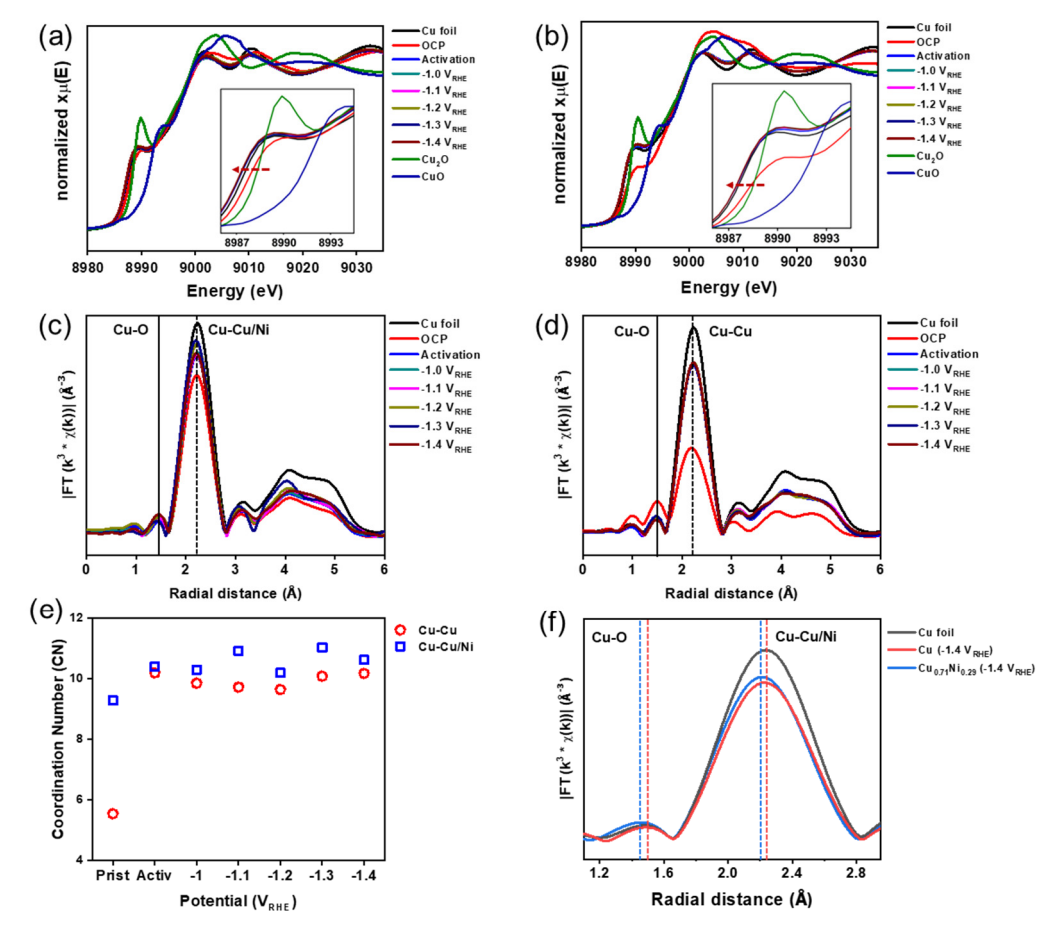


Figure 4. Structural evolution of  $Cu_{0.71}Ni_{0.29}$  catalysts during activation and  $CO_2RR$ . HAADF-STEM and corresponding STEM-EELS elemental maps of pristine  $Cu_{0.71}Ni_{0.29}$  ( $\mathbf{a}-\mathbf{e}$ ),  $Cu_{0.71}Ni_{0.29}$  after activation for 2 h at  $-1.3~V_{RHE}$  ( $\mathbf{f}-\mathbf{j}$ ), and  $Cu_{0.71}Ni_{0.29}$  after  $CO_2RR$  for 5 h ( $\mathbf{k}-\mathbf{m}$ ).



**Figure 5.** (a) Cu K-edge XANES of Cu<sub>0.71</sub>Ni<sub>0.29</sub> under different potentials and standard references of Cu foil, Cu<sub>2</sub>O and CuO, with a zoomed view of the Cu K-edge as inset. (b) Cu K-edge XANES of pure Cu under different potentials and references, with a zoomed view of the Cu K-edge as inset. (c)  $k^3$ -Weighted Cu K-edge *in-situ* EXAFS spectra of Cu<sub>0.71</sub>Ni<sub>0.29</sub> and standard samples. (d)  $k^3$ -Weighted Cu K-edge *in-situ* EXAFS spectra of pure Cu and standard samples. (e) CNs of Cu-metal for Cu<sub>0.71</sub>Ni<sub>0.29</sub> (blue) and pure Cu (red). (f)  $k^3$ -Weighted Cu K-edge *in-situ* EXAFS of Cu foil, pure Cu and Cu<sub>0.71</sub>Ni<sub>0.29</sub> after CO<sub>2</sub> reduction condition.

## 3. Conclusion

In summary, we report the cathodic corrosion-induced structural evolution and enhanced catalytic performance of bimetallic  $Cu_xNi_{1-x}$  NPs for  $CO_2RR$ . The incorporation of Ni, due to its higher oxophilicity, results in surface enrichment that favors the HER prior to activation. Upon cathodic activation, Ni undergoes corrosion, resulting in Ni leaching, Cu exposure, and the formation of a roughened, defect-rich surface. This structural evolution significantly enhances both  $CO_2RR$  activity and  $C_{2+}$  selectivity, with  $Cu_{0.71}Ni_{0.29}$  achieving a  $j_{C2+}/j_{H2}$  ratio of 2.1 and a FE of 42.5% for  $C_{2+}$  products at -1.4 V<sub>RHE</sub>, compared to just 24.1% for pure Cu NPs. *In-situ* and *ex-situ* structural analyses reveal that the Cu in  $Cu_{0.71}Ni_{0.29}$  is less oxidized than in pure Cu and is fully reduced upon activation, confirming Ni's protective effect. Changes in Cu morphology and coordination environment suggest that cathodic corrosion optimizes catalyst performance through the synergistic effects of Ni leaching, Cu reduction, and trace amounts of Ni residue.

Materials: The **Supplementary** Supplementary Materials downloaded https://www.sciltp.com/journals/mi/2024/1/562/s1. Figure S1. TEM images and size distribution of (a,b) Cu; (c,d) Cu<sub>0.81</sub>Ni<sub>0.19</sub>; (e,f) Cu<sub>0.71</sub>Ni<sub>0.29</sub>; (g,h) Cu<sub>0.63</sub>Ni<sub>0.37</sub>; (i,j) Cu<sub>0.39</sub>Ni<sub>0.61</sub> and (k,l) Ni NPs. Figure S2. XRD patterns from 30 to 80 degree of Cu<sub>x</sub>Ni<sub>1-x</sub> with Cu and Ni references. Figure S3. Optimization of the activation step for pure Cu. (a) No activation step. (b) Activation at -1.0 V<sub>RHE</sub>. (c) Activation at −1.1 V<sub>RHE</sub>. (d) Activation at −1.2 V<sub>RHE</sub>. (e) C<sub>2+</sub> products FE. Figure S4. Optimization of the Activation step for Cu<sub>0.81</sub>Ni<sub>0.19</sub>. (a) No activation step. (b) Activation at -1.2 V<sub>RHE</sub>. (c) Activation at -1.3 V<sub>RHE</sub>. (d) Activation at -1.4 V<sub>RHE</sub>. (e) C<sub>2+</sub> products FE. Figure S5. Optimization of the Activation step for Cu<sub>0.71</sub>Ni<sub>0.29</sub>. (a) No activation step. (b) Activation at -1.2 V<sub>RHE</sub>. (c) Activation at -1.3 V<sub>RHE</sub>. (d) Activation at -1.4 V<sub>RHE</sub>. (e) C<sub>2+</sub> products FE. Figure S6. Optimization of the Activation step for Cu<sub>0.63</sub>Ni<sub>0.37</sub>. (a) No activation step. (b) Activation at -1.0 V<sub>RHE</sub>. (c) Activation at -1.1 V<sub>RHE</sub>. (d) Activation at -1.2 V<sub>RHE</sub>. (e) C<sub>2+</sub> products FE. Figure S7. Optimization of the Activation step for Cu<sub>0.39</sub>Ni<sub>0.61</sub>. (a) No activation step. (b) Activation at -1.1 V<sub>RHE</sub>. (c) Activation at -1.2 V<sub>RHE</sub>. (d) Activation at -1.3 V<sub>RHE</sub>. (e) C<sub>2+</sub> products FE. Figure S8. Geometric surface area-normalized current density of  $Cu_xNi_{1-x}$  during  $CO_2RR$ . (a) Partial current density of  $C_{2+}$  products ( $j_{C2+}$ ) at different applied potential. (b) Partial current density of H<sub>2</sub> (j<sub>H2</sub>) at different applied potential. Figure S9. FEs of H<sub>2</sub>, C<sub>1</sub> and

C<sub>2+</sub> for Cu<sub>x</sub>Ni<sub>1-x</sub> before (top) and after (bottom) activation at optimized potential. Figure S10. Composition change and Ni leaching percentage of Cu<sub>0.71</sub>Ni<sub>0.29</sub> under different activation potentials. (The black and blue line are the composition change of Cu and Ni, respectively; the red line is the Ni leaching percentage). Figure S11. HAADF-STEM and corresponding STEM-EELS elemental maps of pure Cu. (a-c) Before activation. (d,e) After activation for 2 h. (g-i) After CO<sub>2</sub>RR for 5 h. Figure S12. Comparison in  $k^3$ -Weighted Cu K-edge *in-situ* EXAFS spectra of pure Cu and Cu<sub>0.71</sub>Ni<sub>0.29</sub> at OCP and after activation at their optimized activation potential. Figure S13. (a) XANES of Cu<sub>0.71</sub>Ni<sub>0.29</sub>, Ni scan. (b) Fourier Transformed EXAFS of Cu<sub>0.71</sub>Ni<sub>0.29</sub>, Ni scan. (c) CN of Cu<sub>0.71</sub>Ni<sub>0.29</sub>, Ni scan. Figure S14. (a-h) Fourier Transformed EXAFS fitting of Cu<sub>0.71</sub>Ni<sub>0.29</sub> at different activation potential, and Cu foil. Figure S15. Fourier Transformed EXAFS fitting of pure Cu at different activation potentials. Figure S16. Fourier Transformed EXAFS fitting of Cu<sub>0.71</sub>Ni<sub>0.29</sub>, Ni scan and Ni foil. Figure S17. EXAFS oscillation functions at the Cu K-edge of Cu<sub>0.71</sub>Ni<sub>0.29</sub> at different conditions and Cu foil reference. Figure S18. EXAFS oscillation functions at the Cu K-edge of pure Cu at different conditions and Cu foil reference. Table S1. Sizes of Cu<sub>x</sub>Ni<sub>1-x</sub> NPs. Table S2. C<sub>2+</sub> FE in the optimization of the activation step for pure Cu (the optimized condition is highlighted). Table S3. C2+ FE in the optimization of the activation step for pure Cu<sub>0.81</sub>Ni<sub>0.19</sub> (the optimized condition is highlighted). Table S4. C<sub>2+</sub> FE in the optimization of the activation step for pure Cu<sub>0.71</sub>Ni<sub>0.29</sub> (the optimized condition is highlighted). Table S5. C<sub>2+</sub> FE in the optimization of the activation step for pure Cu<sub>0.63</sub>Ni<sub>0.37</sub> (the optimized condition is highlighted). Table S6. C<sub>2+</sub> FE in the optimization of the activation step for pure Cu<sub>0.39</sub>Ni<sub>0.61</sub> (the optimized condition is highlighted). Table S7. Atomic composition of Figures 4 and S11. Table S8. Fitting parameters of Cu<sub>0.71</sub>Ni<sub>0.29</sub>, Cu scan. Table S9. Fitting parameter of pure Cu, Cu scan. Table S10. Fitting parameters of Cu<sub>0.71</sub>Ni<sub>0.29</sub>, Ni scan.

**Author Contributions:** W.S.: data curation, investigation, writing, and revising draft. B.M.: data curation, investigation, methodology. M.W.: investigation. X.H.: visualization. Q.G.: methodology. S.H.: methodology, investigation. H.Z. (Hua Zhou): methodology. H.Z. (Huiyuan Zhu): conceptualization and supervision. All authors have read and agreed to the published version of the manuscript.

Funding: This work was supported by the US National Science Foundation (CHE-2332802).

**Data Availability Statement:** The authors declare that the data supporting the findings of this study are available from the corresponding author, H. Zhu, upon reasonable request.

**Acknowledgements:** This research used Electron Microscopy facility of the Center for Functional Nanomaterials (CFN), which is a U.S. Department of Energy Office of Science User Facility, at Brookhaven National Laboratory under Contract No. DE-SC0012704. XAS was done at 12BM. This research used resources of the Advanced Photon Source; a U.S. Department of Energy (DOE) Office of Science User Facility operated for the DOE Office of Science by Argonne National Laboratory under Contract No. DE-AC02-06CH11357.

**Conflicts of Interest:** The authors declare no conflict of financial interest.

#### References

- 1. Wu, J.; Huang, Y.; Ye, W.; Li, Y. CO<sub>2</sub> reduction: From the electrochemical to photochemical approach. *Adv. Sci.* **2017**, *4*, 1700194.
- 2. Zhang, L.; Zhao, Z.J.; Gong, J. Nanostructured materials for heterogeneous electrocatalytic CO<sub>2</sub> reduction and their related reaction mechanisms. *Angew. Chem. Int. Ed.* **2017**, *56*, 11326–11353.
- 3. Bushuyev, O.S.; De Luna, P.; Dinh, C.T.; Tao, L.; Saur, G.; van de Lagemaat, J.; Kelley, S.O.; Sargent, E.H. What should we make with CO<sub>2</sub> and how can we make it? *Joule* **2018**, *2*, 825–832.
- 4. Garza, A.J.; Bell, A.T.; Head-Gordon, M. Mechanism of CO<sub>2</sub> reduction at copper surfaces: Pathways to C<sub>2</sub> products. *ACS. Catal.* **2018**, *8*, 1490–1499.
- 5. Nitopi, S.; Bertheussen, E.; Scott, S.B.; Liu, X.; Engstfeld, A.K.; Horch, S.; Seger, B.; Stephens, I.E.L.; Chan, K.; Hahn, C.; et al. Progress and perspectives of electrochemical CO<sub>2</sub> reduction on copper in aqueous electrolyte. *Chem. Rev.* **2019**, 119, 7610–7672.
- 6. Kuhl, K.P.; Hatsukade, T.; Cave, E.R.; Abram, D.N.; Kibsgaard, J.; Jaramillo, T.F. Electrocatalytic conversion of carbon dioxide to methane and methanol on transition metal surfaces. *J. Am. Chem. Soc.* **2014**, *136*, 14107–14113.
- 7. Bagger, A.; Ju, W.; Varela, A.S.; Strasser, P.; Rossmeisl, J. Electrochemical CO<sub>2</sub> reduction: A classification problem. *Chemphyschem* **2017**, *18*, 3266–3273.
- 8. Gao, D.; Arán-Ais, R.M.; Jeon, H.S.; Roldan Cuenya, B. Rational catalyst and electrolyte design for CO<sub>2</sub> electroreduction towards multicarbon products. *Nat. Catal.* **2019**, *2*, 198–210.
- 9. Zhao, J.; Xue, S.; Barber, J.; Zhou, Y.; Meng, J.; Ke, X. An overview of Cu-based heterogeneous electrocatalysts for CO<sub>2</sub> reduction. *J. Mater. Chem. A* **2020**, *8*, 4700–4734.
- 10. Kuhl, K.P.; Cave, E.R.; Abram, D.N.; Jaramillo, T.F. New insights into the electrochemical reduction of carbon dioxide on metallic copper surfaces. *Energy Environ. Sci.* **2012**, *5*, 7050–7059.
- 11. Zheng, Y.; Vasileff, A.; Zhou, X.; Jiao, Y.; Jaroniec, M.; Qiao, S.Z. Understanding the roadmap for electrochemical reduction of CO<sub>2</sub> to multi-carbon oxygenates and hydrocarbons on copper-based catalysts. *J. Am. Chem. Soc.* **2019**, *141*, 7646–7659.
- 12. Zhao, R.; Ding, P.; Wei, P.; Zhang, L.; Liu, Q.; Luo, Y.; Li, T.; Lu, S.; Shi, X.; Gao, S.; et al. Recent progress in electrocatalytic methanation of CO<sub>2</sub> at ambient conditions. *Adv. Funct. Mater.* **2021**, *31*, 2009449.

- 13. Okatenko, V.; Loiudice, A.; Newton, M.A.; Stoian, D.C.; Blokhina, A.; Chen, A.N.; Rossi, K.; Buonsanti, R. Alloying as a strategy to boost the stability of copper nanocatalysts during the electrochemical CO<sub>2</sub> reduction reaction. *J. Am. Chem. Soc.* **2023**, *145*, 5370–5383.
- 14. Song, H.; Tan, Y.C.; Kim, B.; Ringe, S.; Oh, J. Tunable product selectivity in electrochemical CO<sub>2</sub> reduction on well-mixed Ni-Cu alloys. *ACS Appl. Mater. Interfaces* **2021**, *13*, 55272–55280.
- 15. Wu, Z.-Z.; Gao, F.-Y.; Gao, M.-R. Regulating the oxidation state of nanomaterials for electrocatalytic CO<sub>2</sub> reduction. *Energy Environ. Sci.* **2021**, *14*, 1121–1139.
- 16. Favaro, M.; Xiao, H.; Cheng, T.; Goddard, W.A., 3rd; Yano, J.; Crumlin, E.J. Subsurface oxide plays a critical role in CO<sub>2</sub> activation by Cu(111) surfaces to form chemisorbed CO<sub>2</sub>, the first step in reduction of CO<sub>2</sub>. *Proc. Natl. Acad. Sci. USA* **2017**, *114*, 6706–6711.
- 17. Gu, Z.; Shen, H.; Chen, Z.; Yang, Y.; Yang, C.; Ji, Y.; Wang, Y.; Zhu, C.; Liu, J.; Li, J.; et al. Efficient electrocatalytic CO<sub>2</sub> reduction to C<sub>2+</sub> alcohols at defect-site-rich Cu surface. *Joule* **2021**, *5*, 429–440.
- 18. Vasileff, A.; Xu, C.; Jiao, Y.; Zheng, Y.; Qiao, S.-Z. Surface and interface engineering in copper-based bimetallic materials for selective CO<sub>2</sub> electroreduction. *Chem.* **2018**, *4*, 1809–1831.
- 19. Du, C.; Mills, J.P.; Yohannes, A.G.; Wei, W.; Wang, L.; Lu, S.; Lian, J.X.; Wang, M.; Guo, T.; Wang, X.; et al. Cascade electrocatalysis via AgCu single-atom alloy and Ag nanoparticles in CO<sub>2</sub> electroreduction toward multicarbon products. *Nat. Commun.* **2023**, *14*, 6142.
- 20. Kim, D.; Resasco, J.; Yu, Y.; Asiri, A.M.; Yang, P. Synergistic geometric and electronic effects for electrochemical reduction of carbon dioxide using gold-copper bimetallic nanoparticles. *Nat. Commun.* **2014**, *5*, 4948.
- 21. Chen, C.; Li, Y.; Yu, S.; Louisia, S.; Jin, J.; Li, M.; Ross, M.B.; Yang, P. Cu-Ag tandem catalysts for high-rate CO<sub>2</sub> electrolysis toward multicarbons. *Joule* **2020**, *4*, 1688–1699.
- 22. Iyengar, P.; Kolb, M.J.; Pankhurst, J.R.; Calle-Vallejo, F.; Buonsanti, R. Elucidating the facet-dependent selectivity for CO<sub>2</sub> electroreduction to ethanol of Cu–Ag tandem catalysts. *ACS Catal.* **2021**, *11*, 4456–4463.
- 23. Clark, E.L.; Hahn, C.; Jaramillo, T.F.; Bell, A.T. Electrochemical CO<sub>2</sub> reduction over compressively strained CuAg surface alloys with enhanced multi-carbon oxygenate selectivity. *J. Am. Chem. Soc.* **2017**, *139*, 15848–15857.
- 24. Chang, C.J.; Lin, S.C.; Chen, H.C.; Wang, J.; Zheng, K.J.; Zhu, Y.; Chen, H.M. Dynamic reoxidation/reduction-driven atomic interdiffusion for highly selective CO<sub>2</sub> reduction toward methane. *J. Am. Chem. Soc.* **2020**, *142*, 12119–12132.
- 25. Huang, J.; Hormann, N.; Oveisi, E.; Loiudice, A.; De Gregorio, G.L.; Andreussi, O.; Marzari, N.; Buonsanti, R. Potential-induced nanoclustering of metallic catalysts during electrochemical CO<sub>2</sub> reduction. *Nat. Commun.* **2018**, *9*, 3117.
- 26. Lai, W.; Ma, Z.; Zhang, J.; Yuan, Y.; Qiao, Y.; Huang, H. Dynamic evolution of active sites in electrocatalytic CO<sub>2</sub> reduction reaction: Fundamental understanding and recent progress. *Adv. Funct. Mater.* **2022**, *32*, 2111193.
- Vavra, J.; Ramona, G.P.L.; Dattila, F.; Kormányos, A.; Priamushko, T.; Albertini, P.P.; Loiudice, A.; Cherevko, S.; Lopéz, N.; Buonsanti, R. Solution-based Cu<sup>+</sup> transient species mediate the reconstruction of copper electrocatalysts for CO<sub>2</sub> reduction. *Nat. Catal.* 2024, 7, 89–97.
- Lee, S.H.; Lin, J.C.; Farmand, M.; Landers, A.T.; Feaster, J.T.; Aviles Acosta, J.E.; Beeman, J.W.; Ye, Y.; Yano, J.; Mehta, A.; et al. Oxidation state and surface reconstruction of Cu under CO<sub>2</sub> reduction conditions from in situ X-ray characterization. J. Am. Chem. Soc. 2021, 143, 588–592.
- 29. Kim, Y.G.; Baricuatro, J.H.; Javier, A.; Gregoire, J.M.; Soriaga, M.P. The evolution of the polycrystalline copper surface, first to Cu(111) and then to Cu(100), at a fixed CO<sub>2</sub>RR potential: A study by operando EC-STM. *Langmuir* **2014**, *30*, 15053–15056.
- Delmo, E.P.; Wang, Y.; Song, Y.; Zhu, S.; Zhang, H.; Xu, H.; Li, T.; Jang, J.; Kwon, Y.; Wang, Y.; et al. In Situ infrared spectroscopic evidence of enhanced electrochemical CO<sub>2</sub> reduction and C-C coupling on oxide-derived copper. *J. Am. Chem. Soc.* 2024, 146, 1935–1945.
- 31. Vavra, J.; Shen, T.H.; Stoian, D.; Tileli, V.; Buonsanti, R. Real-time monitoring reveals dissolution/redeposition mechanism in copper nanocatalysts during the initial stages of the CO<sub>2</sub> reduction reaction. *Angew. Chem. Int. Ed.* **2021**, 60, 1347–1354.
- 32. Chen, P.C.; Chen, C.; Yang, Y.; Maulana, A.L.; Jin, J.; Feijoo, J.; Yang, P. Chemical and structural evolution of AgCu catalysts in electrochemical CO<sub>2</sub> reduction. *J. Am. Chem. Soc.* **2023**, *145*, 10116–10125.
- 33. Jeon, H.S.; Timoshenko, J.; Scholten, F.; Sinev, I.; Herzog, A.; Haase, F.T.; Roldan Cuenya, B. Operando insight into the correlation between the structure and composition of CuZn nanoparticles and their selectivity for the electrochemical CO<sub>2</sub> reduction. *J. Am. Chem. Soc.* **2019**, *141*, 19879–19887.
- Gao, Q.; Ju, Y.M.; An, D.; Gao, M.R.; Cui, C.H.; Liu, J.W.; Cong, H.P.; Yu, S.H. Shape-controlled synthesis of monodisperse PdCu nanocubes and their electrocatalytic properties. *ChemSusChem* 2013, 6, 1878–1882.
- 35. Wang, Y.; Xu, A.; Wang, Z.; Huang, L.; Li, J.; Li, F.; Wicks, J.; Luo, M.; Nam, D.H.; Tan, C.S.; et al. Enhanced nitrate-to-ammonia activity on copper-nickel alloys via tuning of intermediate adsorption. *J. Am. Chem. Soc.* **2020**, *142*, 5702–5708.

- 36. Liu, S.; Li, Y.; Wang, D.; Xi, S.; Xu, H.; Wang, Y.; Li, X.; Zang, W.; Liu, W.; Su, M.; et al. Alkali cation-induced cathodic corrosion in Cu electrocatalysts. *Nat. Commun.* **2024**, *15*, 5080.
- 37. McCafferty, E. Introduction to Corrosion Science; Springer: New York, NY, USA, 2010; pp. 111–112.
- 38. Hersbach, T.J.P.; Koper, M.T.M. Cathodic corrosion: 21st century insights into a 19th century phenomenon. *Curr. Opin. Electrochem.* **2021**, *26*, 100653.
- 39. Nong, H.N.; Reier, T.; Oh, H.-S.; Gliech, M.; Paciok, P.; Vu, T.H.T.; Teschner, D.; Heggen, M.; Petkov, V.; Schlögl, R.; et al. A unique oxygen ligand environment facilitates water oxidation in hole-doped IrNiOx core–shell electrocatalysts. *Nat. Catal.* **2018**, *1*, 841–851.
- Lin, S.C.; Chang, C.C.; Chiu, S.Y.; Pai, H.T.; Liao, T.Y.; Hsu, C.S.; Chiang, W.H.; Tsai, M.K.; Chen, H.M. Operando time-resolved X-ray absorption spectroscopy reveals the chemical nature enabling highly selective CO<sub>2</sub> reduction. *Nat. Commun.* 2020, 11, 3525.
- 41. Pan, H.; Barile, C.J. Bifunctional nickel and copper electrocatalysts for CO<sub>2</sub> reduction and the oxygen evolution reaction. *J. Mater. Chem. A* **2020**, *8*, 1741–1748.